

SCIENTIFIC REPORTS

OPEN

Top-down GaN nanowire transistors with nearly zero gate hysteresis for parallel vertical electronics

Muhammad Fahlesa Fatahilah^{1,2}, Feng Yu^{1,2}, Klaas Strempe^{1,2}, Friedhard Römer⁴, Dario Maradan³, Matteo Meneghini⁵, Andrey Bakin^{1,2}, Frank Hohls³, Hans Werner Schumacher³, Bernd Witzigmann⁴, Andreas Waag^{1,2} & Hutomo Suryo Wasisto^{1,2}

This paper reports on the direct qualitative and quantitative performance comparisons of the field-effect transistors (FETs) based on vertical gallium nitride nanowires (GaN NWs) with different NW numbers (i.e., 1–100) and diameters (i.e., 220–640 nm) fabricated on the same wafer substrate to prove the feasibility of employing the vertical 3D architecture concept towards massively parallel electronic integration, particularly for logic circuitry and metrological applications. A top-down approach combining both inductively coupled plasma dry reactive ion etching (ICP-DRIE) and wet chemical etching is applied in the realization of vertically aligned GaN NWs on metalorganic vapor-phase epitaxy (MOVPE)-based GaN thin films with specific doping profiles. The FETs are fabricated involving a stack of *n-p-n* GaN layers with embedded inverted *p*-channel, top drain bridging contact, and wrap-around gating technology. From the electrical characterization of the integrated NWs, a threshold voltage (V_{th}) of (6.6 ± 0.3) V is obtained, which is sufficient for safely operating these devices in an enhancement mode (E-mode). Aluminium oxide (Al_2O_3) grown by atomic layer deposition (ALD) is used as the gate dielectric material resulting in nearly-zero gate hysteresis (i.e., forward and backward sweep V_{th} shift (ΔV_{th}) of ~ 0.2 V). Regardless of the required device processing optimization for having better linearity profile, the upscaling capability of the devices from single NW to NW array in terms of the produced currents could already be demonstrated. Thus, the presented concept is expected to bridge the nanoworld into the macroscopic world, and subsequently paves the way to the realization of innovative large-scale vertical GaN nanoelectronics.

Since the invention of the first integrated circuit (IC) in 1958, planar metal-oxide semiconductor field-effect transistors (MOSFETs) based on silicon have been dominating in the global microelectronics industry and continuously used to build electronic devices, such as modern microprocessors, which up-to-date can integrate more than one billion transistors on a single chip^{1–3}. The raised challenges following this microelectronic revolution are still how to fabricate the transistors more efficiently by keeping the smallest possible footprint and how to better exploit the devices containing billions of transistors. Even though the electronic engineers and scientists have attempted to further miniaturize and to put more transistors on it as well as to improve their performance, the technological bottleneck still occurs as the available active area or footprint of the whole device at a certain point is constrained, leading to the limitation of the integrated electronic building blocks. Therefore, although the development of microelectronics and the following enhancement in circuit performance have generally been driven by the downscaling of the basic electronic component (i.e., the MOSFET), it has faced physical limitations

¹Institute of Semiconductor Technology (IHT), Technische Universität Braunschweig, Hans-Sommer-Straße 66, D-38106, Braunschweig, Germany. ²Laboratory for Emerging Nanometrology (LENA), Technische Universität Braunschweig, Langer Kamp 6, D-38106, Braunschweig, Germany. ³Physikalisch-Technische Bundesanstalt (PTB), Bundesallee 100, D-38116, Braunschweig, Germany. ⁴Computational Electronics and Photonics (CEP), University of Kassel, Wilhelmshöher Allee 71, D-34121, Kassel, Germany. ⁵Department of Information Engineering, University of Padua, 35131, Padua, Italy. Correspondence and requests for materials should be addressed to M.F.F. (email: m.fatahilah@tu-braunschweig.de) or H.S.W. (email: h.wasisto@tu-braunschweig.de)

of nanoscale transistor operation, which then leads to the research and development of more innovative MOSFET architectures, e.g., to improve electrostatic control of the channel. Thus, several novel approaches have been investigated including the usage of other semiconductor materials (e.g., silicon carbide (SiC)⁴ and gallium nitride (GaN)^{5–7} for specific applications (e.g., in high temperature and power switching devices), planar 3D nanostructures (e.g., horizontal nanowire (NW) transistors)^{8,9}, and vertical 3D architectures (e.g., FinFET, NW FET, and tri-gate architectures)^{10–14}.

Among others, GaN transistors provide prospects for making monolithically integrated electronics-photonics platforms because of their direct wide band gap, even though the already realized devices are still in a planar architecture^{15,16}. As the figure of merits for semiconductor power devices, the high breakdown voltage (BV) and low on resistance (R_{on}) are required, in which $BV > 800$ V and $R_{on} \approx 0.36$ m Ω cm² can be obtained by vertical GaN FinFET based on bulk GaN wafer¹⁴. In quantum engineered transistors and logic applications, this vertical method also gives a new strategy towards higher performance and integration of *p*- and *n*-channel transistors^{17,18}. From our point of view, the vertical 3D architecture has become more attractive because it provides more advantages: (1) it can minimize the current collapse, thanks to the absence of surface-related trapping phenomena; (2) the gate length (L) is not limited by lithography process; (3) gating technology can be flexibly designed (e.g., wrap around gate); (4) vertical parallel current paths and collection can be obtained on a small footprint for high scalability; (5) better thermal performance, at which the maximum temperature is close to top part of NWs, brought potential to achieve more power density; and (6) contrary to lateral devices, where breakdown voltage scales with area (and cost), in vertical devices the breakdown voltage is only dependent on the thickness/properties of the epitaxial stacks^{13,19–25}.

In the last few years, several vertical electronic devices based on semiconductor NWs (e.g., Si and GaN) have been demonstrated with different types of transistors, and only a few of them concern about the direct device scaling behavior as affected by the modified number and diameter of NWs^{26–28}. The diameter size and doping concentration of *n-n-n* or *n-i-n* GaN epitaxial NWs were reported to be able to determine the operation modes of the GaN FETs (normally-off or normally-on)^{29,30}. The threshold voltage can be increased by inserting a *p*-channel inside the wire structure instead of *n*-channel^{13,28,30}. Nevertheless, those devices exhibited very large drain current hysteresis during bidirectional gate sweep, which is assumed to be due to the unintentionally introduced mobile ions. Meanwhile, for vertical Si FETs, the massively parallel dense NW arrays with wrap around gate structure had been reported to have an improved electrostatic control during device operation, a smaller transistor chip size, and a low leakage current²⁶. However, those nanotransistors were fabricated using electron beam lithography, which definitely lowers their potential to be transferred in batch production because of the higher device processing cost and longer production time. Thus, other lithography techniques (e.g., photolithography, nanoimprint lithography, and colloidal lithography) have been currently employed to produce vertical Si NW arrays, although such production of vertical Si NW FET devices using those techniques has not been demonstrated so far^{31–38}.

In this paper, a direct proof of device current scaling and parallel transistor integration is demonstrated using vertical *n-p-n* GaN NW FETs with almost-zero ΔV_{th} hysteresis that were fabricated using top-down approach (i.e., standard UV-photolithography and hybrid etching processes). Al₂O₃ thin layers fabricated by ALD process using trimethylaluminum and water were employed as gate dielectrics instead of SiO₂ films that are commonly used for Si FETs. Owing to various patterns on the mask, the electrical characteristics of the realized 1-, 9-, and 100-NW FETs with different diameters were extracted and analyzed. In case of the top drain electrode configuration, mesa structures have been added as mechanical support for more robust electrical characterization and circuit integration (e.g., during wire bonding).

Results and Discussion

Figure 1a depicts the 3D device schematic based on the *n-p-n* GaN epi-layer provided in Fig. 1b. The doping concentration of the channel region has a significant impact on the operation mode of the transistors, which influences the threshold voltage. In our devices, the channel is *p*-doped to obtain sufficiently high threshold voltages.

To investigate the scaling behavior of the integrated FETs, devices containing different numbers of NWs were fabricated, i.e., 1, 9, and 100 NWs (Fig. 2a–c). However, for the sake of simplicity, in the next result discussions, the three FET wire diameters of (221 ± 9) nm, (443 ± 7) nm, and (647 ± 8) nm (Fig. 2d–f) are written as 220 nm, 440 nm, and 640 nm, respectively. The formation of smooth sidewalls on vertical *n-p-n* GaN NWs after anisotropic wet chemical etching is explained in detail elsewhere^{13,30,39}. Additionally, it is worthy to mention that the high quality of the etched NW sidewalls is important for the device performance¹⁴.

Figure 3a shows the tested sample containing 1, 9, and 100 NW FETs connected with three probing tips to a source meter unit (SMU). The benefit of using two GaN mesa structures for drain contacts at the both sides of the NW field is the enhanced mechanical support during SMU probe testing or wire bonding process compared to devices with only photoresist or other soft materials underneath the metal pads^{28,40,41}. It should be noted that no additional mask is required during the processing, as the drain pad was formed in line with the first lithography step for creating the NWs at the beginning of device fabrication. Consequently, the pad has the same height as the NWs. Figure 3b–d show the SEM images of fabricated vertical *n-p-n* GaN NW FETs with 1, 9, and 100 NWs including their top drain bridging contacts.

Figure 4a presents the output characteristics of vertical *n-p-n* GaN NW FETs with a diameter of 440 nm and different numbers of 1, 9, and 100 NWs under the gate-source bias (V_{gs}) ranging from 3 to 9 V. For each FET type, five different devices were measured on a single 2-inch epi-GaN wafer. The extracted maximum drain current ($I_{d,max}$) at $V_{gs} = 9$ V demonstrates the linearity in respect to the number of NWs as shown in Table 1. The $I_{d,max}$ and I_{on}/I_{off} of each GaN NW FET scale up with the increasing number of NWs. Thus, it has proven the design suitability for massive parallelization. However, it should be noted that device processing imperfection can provide a deteriorated linearity of the devices, e.g., in the case of device scaling from 9 to 100 NW FETs, where their measured $I_{d,max}$ are (33.5 ± 9.9) μ A and (230.7 ± 59.4) μ A, respectively. The normalized $I_{d,max}$ (i.e., I_{d,max_norm})

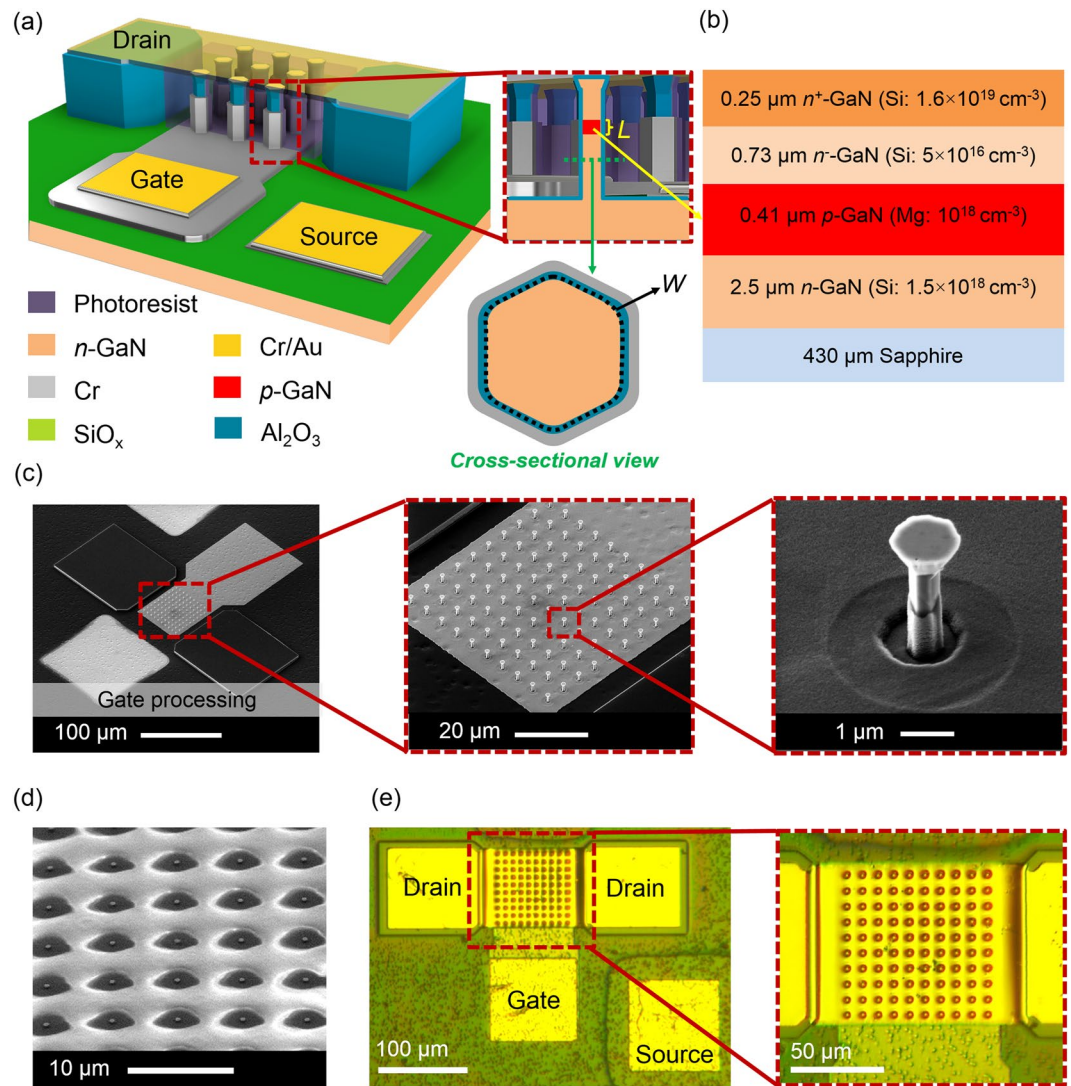


Figure 1. (a) 3D schematics of a 9 *n-p-n* vertical GaN NW FET with L and W as gate length and gate width in inset, respectively, and (b) wafer composition used in this work. Fabrication process steps for creating 1, 9, and 100 NW FETs after (c) Cr gate processing, (d) photoresist filling, short UV exposure, and curing for 30 min at 250 °C, (e) e-beam evaporation of Cr/Au (80/200 nm) and subsequent etch-back process to form metal drain contact on *n-p-n* vertical GaN NW array.

shows similar amounts of current density for FETs with different gate widths (W) and NW numbers, although the values are slightly varied from (1.7 ± 0.4) to $(2.6 \pm 0.9) \mu\text{A}/\mu\text{m}$. The W is defined as the circumference of the single GaN NW, which has values of 0.69 μm , 1.38 μm , 2.01 μm for FETs with NW diameters of 220 nm, 440 nm, 640 nm, respectively.

Those values are obtained by simplifying the cross-sectional geometry of the wire from hexagonal to circular shapes, as the wire dimension is considerably small. The $I_{d,\text{max_norm}}$ can be calculated as follows:

$$I_{d,\text{max_norm}} = \frac{I_{d,\text{max}}}{W \times N} = \frac{I_{d,\text{max}}}{\pi \times D \times N} \quad (1)$$

where D and N are diameter and number of the NWs, respectively. A similar method is used to obtain the normalized transconductance ($g_{m,\text{max_norm}}$), i.e., by dividing the maximum transconductance ($g_{m,\text{max}}$) with $(W \times N)$.

Regardless of the rectifying I-V behavior in lower V_{ds} field and the required contact optimization, the devices can still function in an enhancement mode (E-mode) operation. To improve the Ohmic contact, several solutions are suggested and will be attempted in future, such as usage of other metal materials (e.g., Ti/Al, Ti/Al/Ni/Au, or Ti/Cr/Au) with optimized thickness and annealing processes^{42–45}.

The transfer characteristic is shown in Fig. 4b, plotting I_d as a function of V_{gs} . The average V_{th} values determined by a linear extrapolation of the g_m (Fig. 4c) were (6.4 ± 0.2) V, (6.6 ± 0.3) V, (6.4 ± 0.5) V for the 1, 9, and 100 NW FETs, respectively, which are almost three times higher than the previously reported MOSFETs with c-axis GaN NWs¹³.

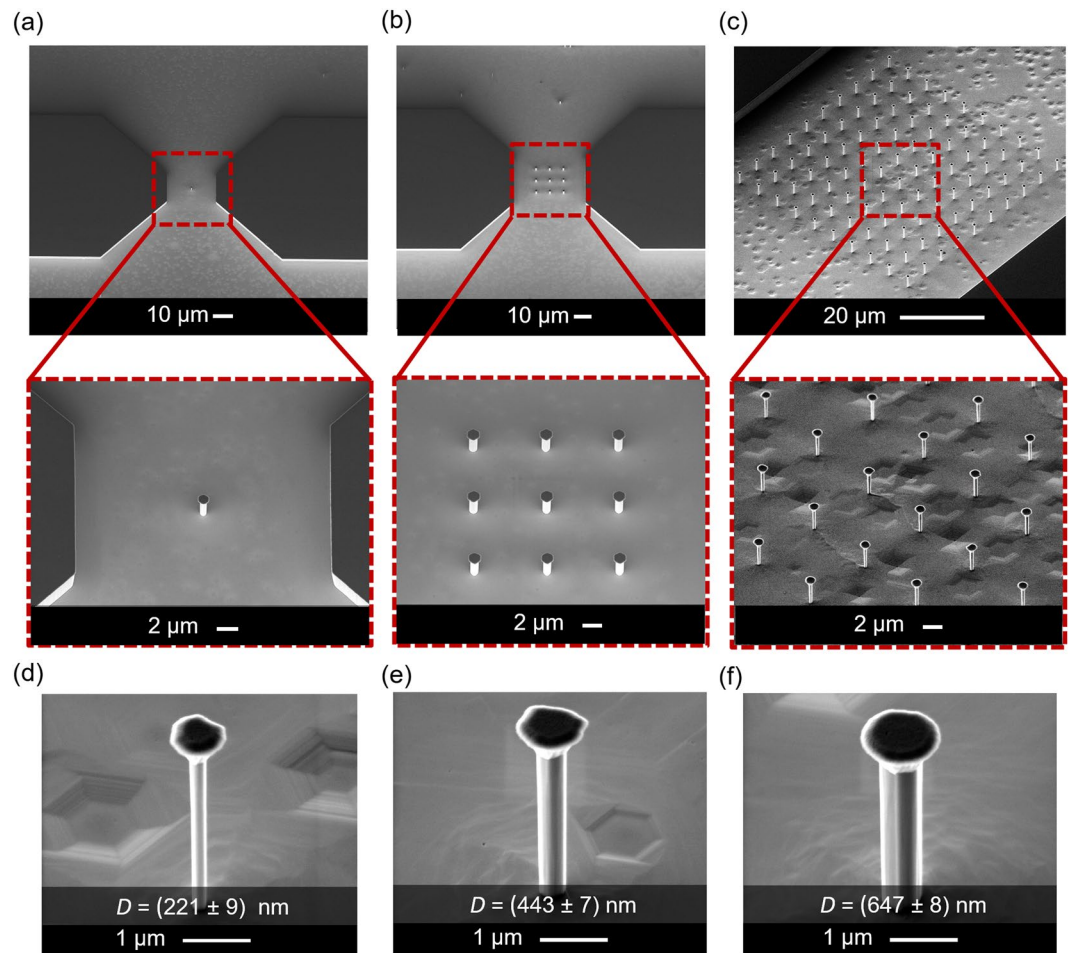


Figure 2. Bird-view SEM images of vertically aligned *n-p-n* GaN nanowire (NW) arrays after ICP-DRIE and wet chemical etching with NW numbers of (a) 1, (b) 9, and (c) 100. Varied wire diameters (D) of (d) (221 ± 9) nm, (e) (443 ± 7) nm, and (f) (647 ± 8) nm were obtained originating from different pattern sizes of the used Cr etching mask.

Compared to the massively parallel vertical Si NW FETs fabricated using e-beam lithography, these GaN NW FETs were believed to provide more stable process, regardless of the required engineering of the interface between the semiconductor and dielectric materials^{26,46,47}. The ON-/OFF current ratios (I_{on}/I_{off}) of up to 10^7 , 10^6 , and 10^5 were achieved for 100, 9, and 1 NW FETs, respectively (see SI Fig. S1), through the logarithmic I_d - V_{gs} curves. Meanwhile, the normalized I_{on}/I_{off} (i.e., I_{on}/I_{off_norm}), which is defined as I_{on}/I_{off} per number of NWs, is found to be similar at values of 10^5 for 1, 9, and 100 NW FETs (see Table 1). Those measured two parameters (I_{on}/I_{off} and I_{on}/I_{off_norm}) have demonstrated the scalability and fabrication quality of the *n-p-n* GaN NW FETs, respectively. The higher I_{on}/I_{off} on 100 NW FETs is reasonable since the $I_{d,max}$ is proportional to number of NWs, in which for this NW FET the value is larger than those on 1 and 9 NW FETs, as depicted in Fig. 4b. The g_{m,max_norm} values (Fig. 4c) were measured as 6.3 mS/mm, 4.1 mS/mm, and 4.7 mS/mm for the 1, 9, and 100 NW FETs, respectively. The oxide capacitances in these FETs are around 4.7 pF, based on capacitive-voltage (C-V) measurements (see SI Fig. S2). Several solutions can be proposed to enhance the g_m , including by decreasing L and increasing the W (i.e., shorter gate channel and larger NW diameter), as well as choosing the proper channel doping concentration design with the purpose of further increasing the electron mobility (μ) in *p*-channel to lower the scattering rate⁴⁸. Review on vertical 3D GaN NW FETs including their important parameters to evaluate the device performances has been recently published elsewhere²⁵.

From Fig. 4d, a gate memory effect or typical hysteresis caused by adsorbates, mobile ions, or interface/oxide traps is not visible in the fabricated devices, which demonstrates a good quality of the used dielectric material (i.e., higher electron affinity and particle density compared to SiO_2)^{13,14,49,50}. In addition, no obvious hysteresis was found on the 1 NW FETs with different diameters and on the 1, 9, 100 NW FETs with diameter of 220 nm (see SI Fig. S3). It should be noted that our previous NW FET devices using SiO_2 gate dielectrics have large gate hysteresis during up-/down- current sweep¹³.

Figure 5a shows the output characteristics of three different single NW FETs with varied diameters (i.e., 220 nm, 440 nm, and 640 nm). The average $I_{d,max}$ values at $V_{gs} = 9$ V from the five conducted measurements exhibit a linear trend, for all diameters with the lowest value found for 220 nm transistor, while the current difference of 7.4 μA was measured between 440 nm and 640 nm transistors. The detailed DC characteristics of the investigated single NW FETs are listed in Table 2.

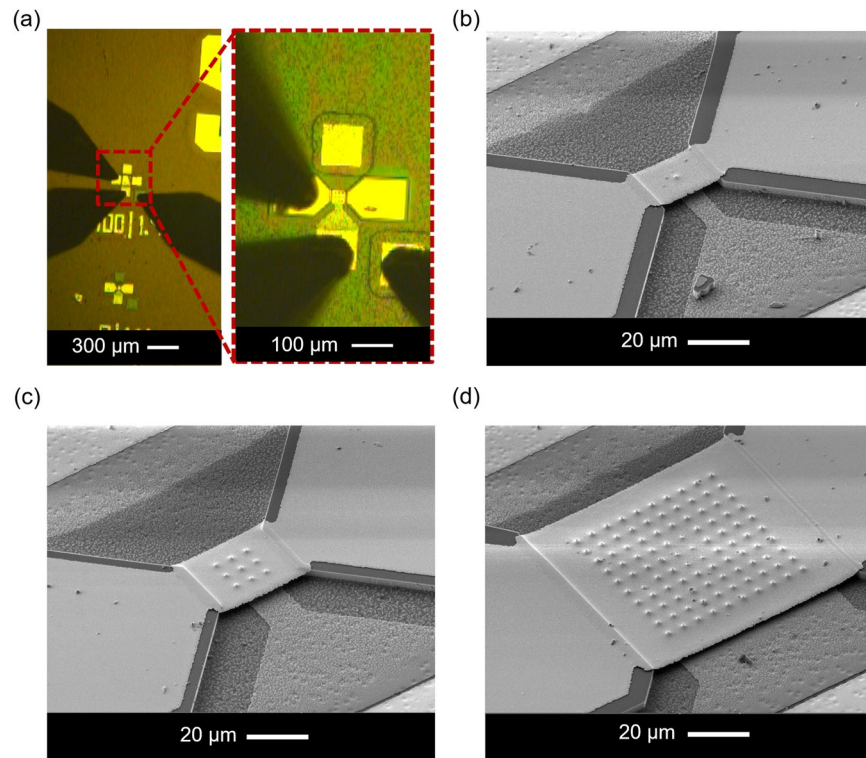


Figure 3. (a) Optical micrograph of a GaN FET device under test using a source meter unit (SMU) and probing tips. SEM images of vertical *n-p-n* GaN NW FETs consisting of (b) 1, (c) 9, and (d) 100 NWs.

The transfer characteristics of the FETs with three different NW diameters are shown in Fig. 5b with an average $V_{th} = (6.4 \pm 0.4)$ V at $V_{ds} = 5$ V. Again, in Fig. 5c, g_{m,max_norm} values were inspected to be 8.8 mS/mm, 6.3 mS/mm, and 7.7 mS/mm for 220 nm, 440 nm, and 640 nm, respectively, with an I_{on}/I_{off} of up to 10^6 (Fig. 5d). The drain leakage ($I_{d,leak}$) below the V_{th} was as low as ~ 10 pA (Fig. 5d) similar to the noise level of the measurement setup (1–10 pA), while the gate dielectric leakage current ($I_{g,leak}$) was observed to be as low as ~ 0.07 nA/NW at $V_{ds} = 5$ V and $V_{gs} = 6$ V for those three different FETs (Fig. 5e). It proves that the high-*k* dielectrics, denser particle, and higher electron affinity of Al_2O_3 ultrathin void-free layer deposited by ALD have excellent properties on suppressing the $I_{d,leak}$ and $I_{g,leak}$ in our transistors⁴⁵. Compared to single NW FETs, the output characteristic performances of 100 NW FETs have more linearity in case of different wire diameters (Fig. 5f).

To understand the phenomena of lower $I_{d,max}$ and higher V_{th} obtained from the developed devices, the effects of gate length (*L*) and surface charge (Q_{sf}) have been further studied by numerical simulations. The value of the gate length extension (L_{ext}) describes the extension of the gate electrode beyond the *p*-channel region and results from the difference between the gate length *L* and the vertical position of the drain side *p-n* junction. The gate length is critical and should be kept as short as possible to limit the electric field in the drift region. A negative Q_{sf} on the nonpolar sidewalls of GaN NWs has been observed in experiments⁵¹. Its primary effect is to increase the threshold voltage of the transfer characteristics. Calibrating the simulations with the transfer characteristics yields the $Q_{sc} = -(3.9 \pm 0.2) \times 10^{11} \text{ cm}^{-2}$ and $L_{ext} = -(21 \pm 4)$ nm for all NW diameters. The gate electrode ends in the *p*-channel near the junction to the drift region (SI Fig. S5a,b calibrated). Figure 6b illustrates a very good agreement of simulation and experiment, which means some parameters in experiment in case of three different diameters of 1 NW FETs should be correct and can be explained by these conducted simulations.

The simulated output characteristics in Fig. 6a show relatively good agreement with the experimental results for the 220 nm and 440 nm NW FETs. However, a rather large difference of the turn-on voltage in the output characteristics of the 640 nm NW device suggests that the gate length value owned by the fabricated FET is probably higher, which is subject to the device processing. This will result in shorter channel length and consequently lower turn-on voltage ($I_d - V_{ds}$), in comparison to that from simulation. Furthermore, the simulations in Fig. 6c,d demonstrate that the $I_d - V_{ds}$ and $I_d - V_{gs}$ curves are very sensitive to L_{ext} . Due to deposition shading and the hexagonal wire shape, the gate metal length varies on the perimeter as depicted by the SEM image of a single wire in Fig. 1c. The variation increases with the diameter explaining the large deviation of the output characteristics for the 640 nm NW FET in Fig. 2a.

Even though the turn-on in the output characteristic may be also caused by imperfect Ohmic source or drain contacts, the simulations suggest that the high threshold and low transconductance can be attributed to the dimensions of the gate electrode. Moreover, surface charging effect has occurred on all FETs, which most probably originates from the impaired quality of the Al_2O_3 gate dielectric layer that has direct contact to GaN NW sidewalls. Nevertheless, all these phenomena need to be further investigated more deeply to understand the surface physics of the used materials from the realized FET devices.

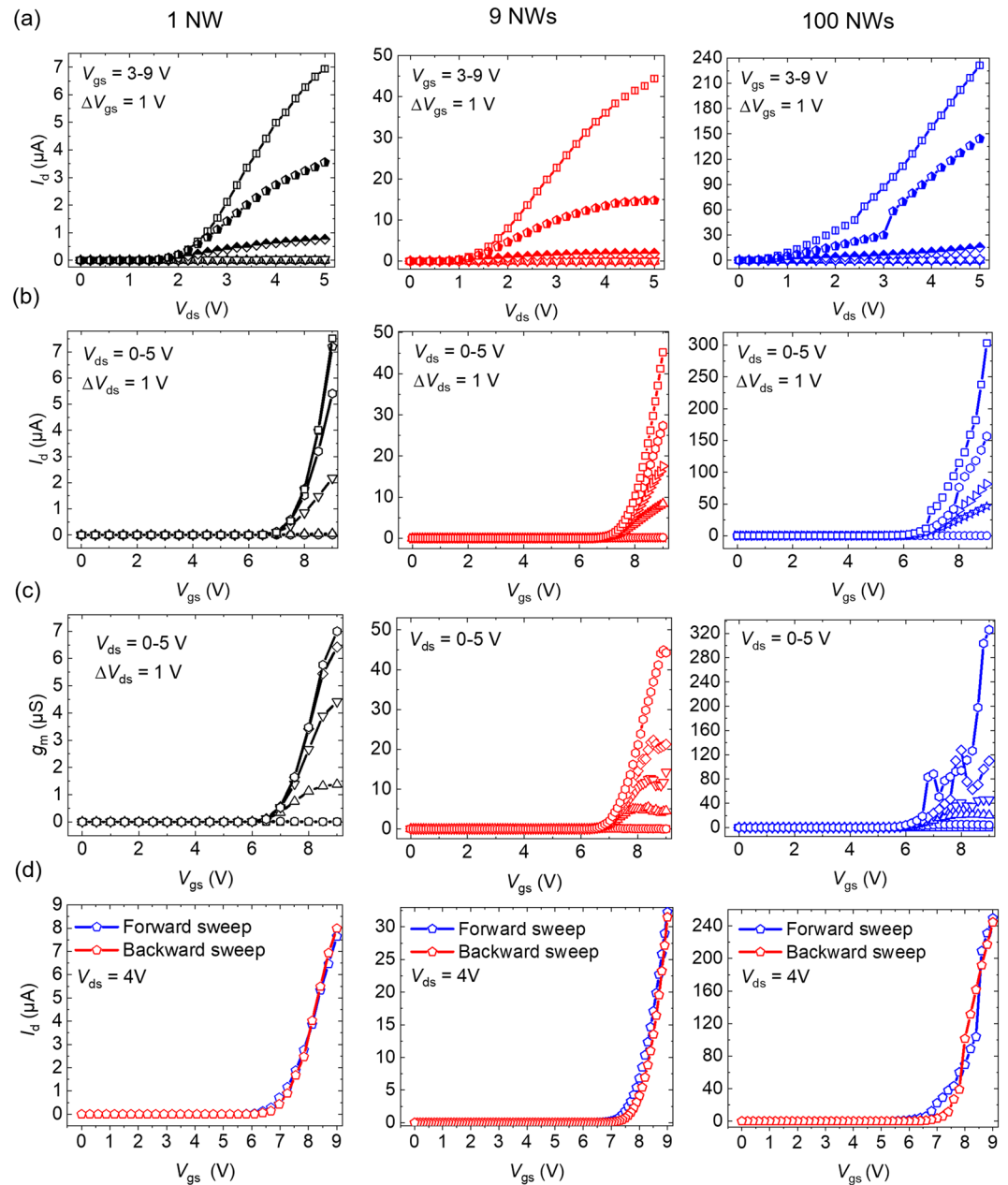


Figure 4. (a) Output characteristic, (b) transfer characteristic, (c) transconductance (g_m), and (d) dual sweep mode transfer characteristic (sweep rate of 0.8–1 V/s) of 1, 9, and 100 *n-p-n* vertical GaN NW FETs with diameter of 440 nm at $V_{ds} = 4$, respectively. All measurements were done in normal ambient condition (room temperature) for at least five sweep cycles on each FET device.

Number of NW (#)	V_{th} (V)	$I_{d,max}$ (μA)	$I_{d,max,norm}$ ($\mu A/\mu m$)	I_{on}/I_{off}	$I_{on}/I_{off,norm}$
1	(6.4 ± 0.2)	(3.2 ± 2.1)	(2.3 ± 1.5)	10^5	10^5
9	(6.6 ± 0.3)	(33.5 ± 9.9)	(2.6 ± 0.9)	10^6	10^5
100	(6.4 ± 0.5)	(230.7 ± 59.4)	(1.7 ± 0.4)	10^7	10^5

Table 1. DC characteristic results of vertical *n-p-n* GaN NW FETs (average value) with NW numbers of 1, 9, and 100 and a diameter of 440 nm.

Figure 6c,d illustrate the effects of the gate length on the output and transfer characteristics for the calibrated surface charge on 220 nm GaN NW FETs. With decreasing gate length, the resistivity increases and the transconductance decreases because the electron depletion in the drift region cannot be lifted by the gate electric field. For a very short gate ending in the *p*-channel region, the gate electric field does not screen the potential barrier at the junction to drift region anymore. Thus, a turn-on voltage in the output characteristics occurs. The negative

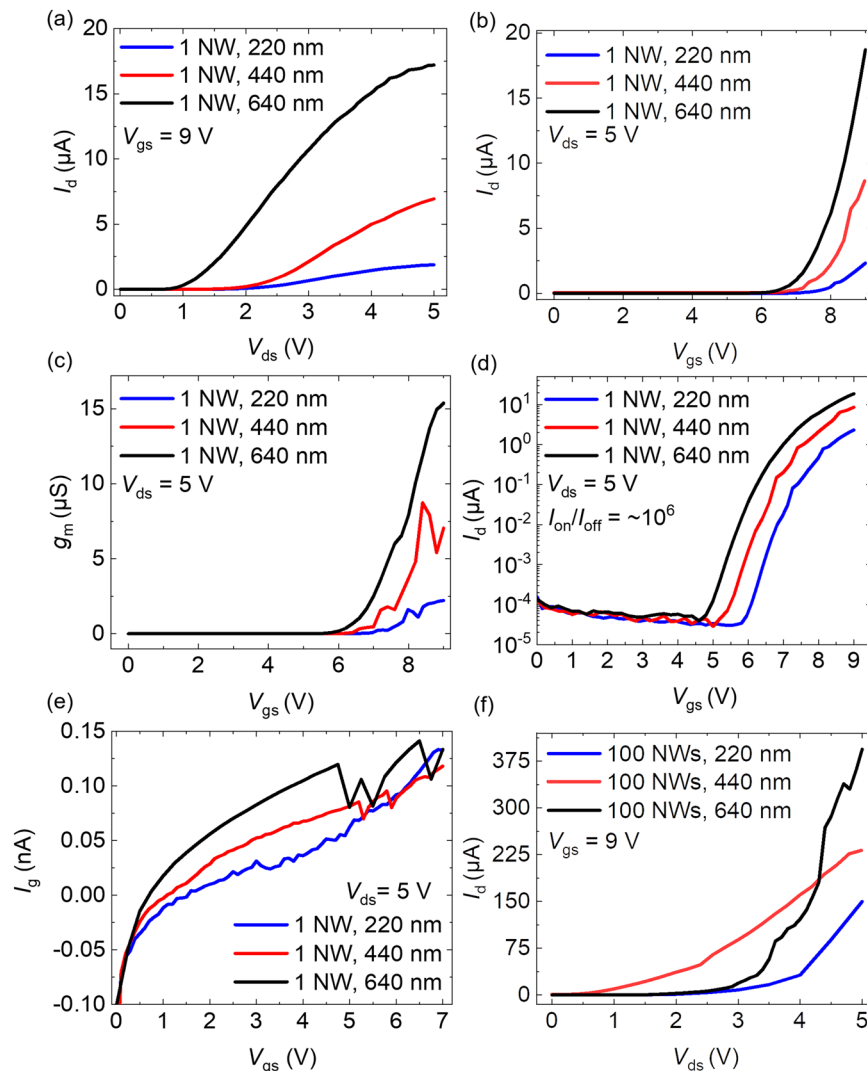


Figure 5. (a) Output characteristic, (b) transfer characteristic, (c) transconductance characteristic, (d) I_{on}/I_{off} characteristic, (e) gate leakage characteristic of 1 NW FETs, and (f) output characteristic of 100 NW FETs with three different diameters (i.e., 220 nm, 440 nm, and 640 nm).

Diameter of NW (nm)	V_{th} (V)	$I_{d,max}$ (μ A)	$I_{d,max,norm}$ (μ A/ μ m)
220	(6.6 ± 0.6)	(2.2 ± 0.8)	(3.2 ± 2.0)
440	(6.4 ± 0.2)	(3.2 ± 2.1)	(2.3 ± 1.5)
640	(6.3 ± 0.3)	(9.5 ± 4.1)	(4.5 ± 2.1)

Table 2. DC characteristic results of single vertical *n-p-n* GaN NW FETs (average value) with three different diameters of 220 nm, 440 nm, and 640 nm.

surface charge does not only increase the threshold voltage as shown in Fig. 6f, but also contributes to the depletion of the drift region, which can be seen from the increase of resistivity in Fig. 6e. With increasing negative surface charge, the junction depletion region extends more into the drift region that contributes to the turn-on voltage in the output characteristics. It is remarkable that for a short gate configuration, the electric field in the drift region near the junction to the channel is larger than the field near the drain region, which exhibits a high resistivity. However, for a long gate architecture, this effect is not found (see SI Fig. S5a,b).

The measured BVs of the 1, 9, and 100 NW FETs were verified from 30–90 V at $V_{gs} = 0$ V as shown in SI Fig. S4. Theoretically, the BV is determined by the length and doping concentration of the drift region. In these devices, the space between drain and gate channel is $\sim 1 \mu$ m, which is much shorter than our previous device having BVs of 54–92 V¹³. However, for improving the device design and performance, several strategies can be proposed for the next transistor generations, e.g., decreasing the Si-doping concentration in the drift region, integrating vertical field-plate structure, and employing longer drift region. The low doped and longer space drift region will reduce the local electric field and thus the BV can be increased^{20,29,52}.

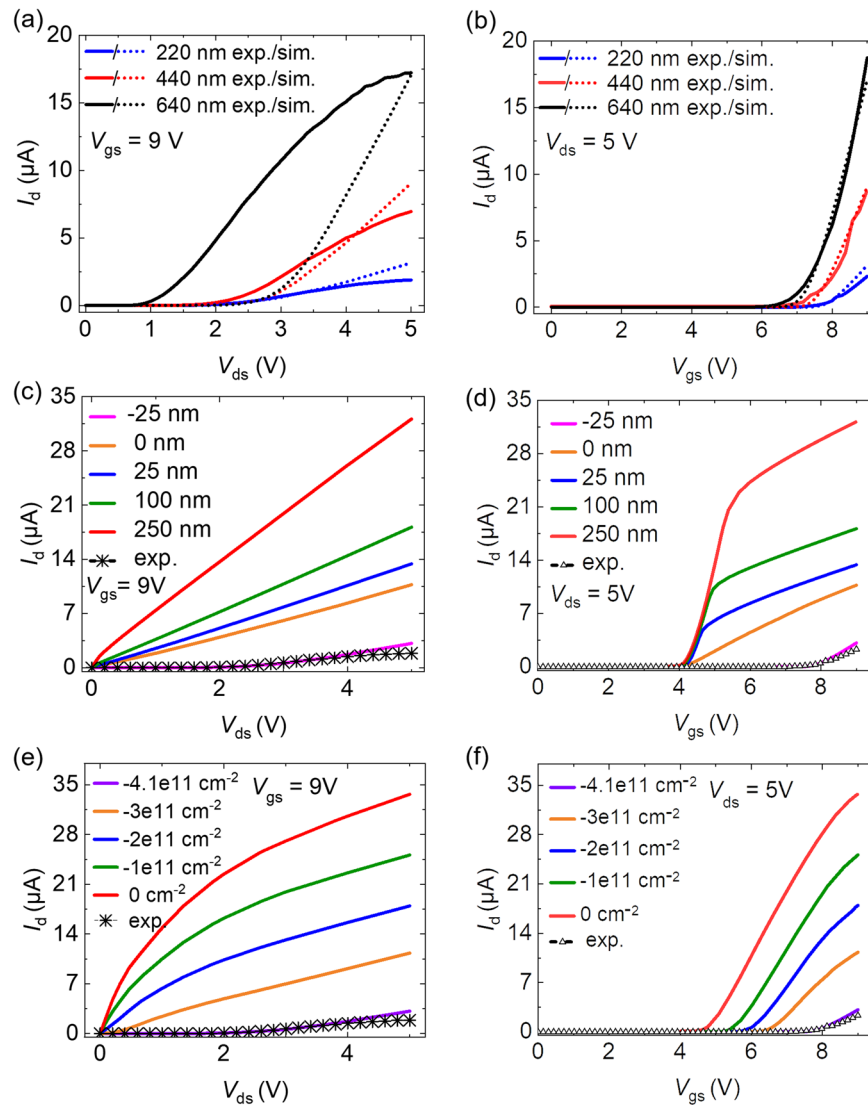


Figure 6. Experimental (exp.) and simulation (sim.) results showing (a) output and (b) transfer characteristics for single NW FETs of different diameters. (c) Simulated output and (d) transfer characteristics of different L_{ext} on single NW FETs with diameter of 220 nm and surface charge $Q_{\text{sc}} = -(3.9 \pm 0.2) \times 10^{11} \text{ cm}^{-2}$. The exp. data are used for comparison, which fit well with simulated results of FET with L_{ext} of -25 nm . (e) Simulated output and (f) transfer characteristics of different Q_{sc} on NW sidewall in case of single NW FETs with diameter of 220 nm and $L_{\text{ext}} = -(21 \pm 4) \text{ nm}$.

In conclusion, E-mode vertical *n-p-n* GaN NW FETs with different properties (i.e., NW numbers and diameters) have been fabricated and demonstrated, proving the feasibility for upscaling the vertical transistors by optimizing the dielectric materials and device designs. The smooth vertical sidewalls of the *n-p-n* NWs have been realized by a hybrid top-down approach involving dry and wet chemical etching techniques. Regardless of the required device processing optimization, the fabricated FETs have exhibited V_{th} of up to $(6.6 \pm 0.3) \text{ V}$ and shown an upscaling $I_{\text{d,max}}$ behavior with increasing NW quantity from 1 to 100 and NW diameter from 220 nm to 640 nm. Through appropriate dielectric passivation material deposited on the entire NWs, the gate hysteresis effect observed in earlier devices could be suppressed to nearly zero. To enhance $I_{\text{d,max}}$, the NW diameter can be further controlled (larger W) and the NW number can be employed ($N > 100$ NWs). These results grant a very promising future design for massively parallel GaN vertical transistors to be used in logic circuitry and metrological applications (i.e., to be extended for single-electron transistors (SETs) providing alternatives for parallel planar GaAs SETs^{53,54}).

Methods

GaN NW array preparation. The NW arrays were fabricated out of epitaxial GaN layers grown by metalorganic vapor-phase epitaxy (MOVPE) on sapphire substrates in a top-down hybrid etching approach. The epitaxial wafer has an *n-p-n* layer stack structure (Fig. 1b). Afterwards, the wafers were patterned by photolithography and lift-off technique with Cr as dry etching mask. Hexagonal-cone GaN nanostructure arrays were obtained by

ICP-DRIE with SF_6 and H_2 gases. Furthermore, KOH-based wet chemical etching was carried out to remove the plasma-induced surface damage of the nanostructures and to shrink the diameter of the hexagonal structures realizing smooth vertical sidewalls. The NW diameters were varied as defined during photolithography to be (221 ± 9) nm, (443 ± 7) nm, and (647 ± 8) nm after ICP-DRIE and wet chemical etching, while the NW height was kept the same at around $3 \mu\text{m}$ ²⁰.

Transistor fabrication. In 3D device processing of vertical GaN NW FETs, highly n -doped GaN was used on top layer of the NWs to improve the quality of the Ohmic contacts. The Mg acceptors in the gate channel (p -channel) of n - p - n GaN NWs were activated by rapid thermal annealing (RTA) at 950°C for 30 s and subsequently at 600°C for 5 min. Furthermore, thermal ALD technique using trimethylaluminum and water was employed to form a ~ 25 nm thick Al_2O_3 gate dielectric layer. To improve the passivation between the GaN layer and the gate metal, a 200 nm thick SiO_x was deposited using e-beam evaporation. The wrap around Cr gate (Fig. 1c) was deposited via tilted e-beam evaporation, using the shadowing effect from the mushroom-like NW shape to prevent any deposition on the upper part of the NWs. Thus, it covered the $0.4 \mu\text{m}$ p -channel area on the GaN epi-layer (Fig. 1b) and is located $1 \mu\text{m}$ below the top mushroom head of NWs (see inset Fig. 1a). The W is the circumference of the NWs with diameters of 220 nm, 440 nm, and 640 nm. For supporting the drain contact, the space between the GaN NWs was filled with photoresist with short UV exposure and cured at around 250°C for 30 min (Fig. 1d). Next, to form an Ohmic contact, a Cr/Au (80/200 nm) layer stack was deposited (see Fig. 1e). Afterwards, this sacrificial polymer could be removed if necessary resulting in top drain bridging contact.

DC characterization. The output and transfer characteristics of FETs were measured by an SMU Keithley 4200-semiconductor characterization system (SCS) at room temperature and under parasitic electric charge protection. Three point-like gold probes with coaxial cables probes were used to enhance the electric transfer between the device and the SMU. All V_{th} and $I_{\text{d,max}}$ values were conducted from five measurements of the same FETs. Hence, the average values and their standard deviations were finally taken.

Simulation Model. The numerical simulations have been carried out with Sentaurus Device using hydrodynamic carrier transport for electrons and drift-diffusion transport for holes. The lattice temperature is 300K for all simulations. The hexagonal NW was approximated by a cylindrical geometry and simulated on a 2D radial cross section using azimuthal expansion. The gate isolation material (Al_2O_3) has been assumed to be crystalline with a permittivity $\varepsilon = 10.2$. A calibration of the gate capacitance was not possible due to the large contribution of the contact capacitance in the experiment (SI Fig. 2). The carrier mobility model incorporates high field saturation of the velocity as well doping dependence⁵⁵. The acceptor doping of the channel region and the donor doping of the drift region are $N_A = 2 \times 10^{18} \text{ cm}^{-3}$ and $N_{\text{D,drift}} = 5 \times 10^{16} \text{ cm}^{-3}$, respectively, and calibrated with experimental results in Fig. 5a,b.

Data Availability

All data generated or analyzed during this study are included in this published article (and its Supplementary Information (SI) files).

References

- Alloati, L. High-Speed Photonics for Side-by-Side Integration with Billion Transistor Circuits in Unmodified CMOS Processes. *Journal of Lightwave Technology* **35**, 1168–1173 (2017).
- Chau, R., Doyle, B., Datta, S., Kavalieros, J. & Zhang, K. Integrated nanoelectronics for the future. *Nature Materials* **6**, 810–812 (2007).
- Zeng, G. & Zeng, S. Study on the Development of the Chip Information Industry Based on Moore's Law. *Journal of Computer and Communications* **05**, 39–47 (2017).
- She, X., Huang, A. Q., Lucia, O. & Ozpineci, B. Review of Silicon Carbide Power Devices and Their Applications. *IEEE Transactions on Industrial Electronics* **64**, 8193–8205 (2017).
- de Paula, W. J. *et al.* A review on gallium nitride switching power devices and applications. in *2017 Brazilian Power Electronics Conference (COBEP)* 1–7 (IEEE, 2017).
- Zhang, Y., Dadgar, A. & Palacios, T. Gallium nitride vertical power devices on foreign substrates: a review and outlook. *Journal of Physics D: Applied Physics* **51**, 273001 (2018).
- De Santi, C., Meneghini, M., Meneghesso, G. & Zanoni, E. Review of dynamic effects and reliability of depletion and enhancement GaN HEMTs for power switching applications. *IET Power Electronics* **11**, 668–674 (2018).
- Huang, Y., Duan, X., Cui, Y. & Lieber, C. M. Gallium Nitride Nanowire Nanodevices. *Nano Letters* **2**, 101–104 (2002).
- Vandenbrouck, S. *et al.* 12 GHz F_{MAX} GaN/AlN/AlGaIn Nanowire MISFET. *IEEE Electron Device Letters* **30**, 322–324 (2009).
- Salahuddin, S., Ni, K. & Datta, S. The era of hyper-scaling in electronics. *Nature Electronics* **1**, 442–450 (2018).
- Amano, H. *et al.* The 2018 GaN power electronics roadmap. *Journal of Physics D: Applied Physics* **51**, 163001 (2018).
- Sabui, G. *et al.* GaN Nanowire Schottky Barrier Diodes. *IEEE Transactions on Electron Devices* **64**, 2283–2290 (2017).
- Yu, F. *et al.* Normally Off Vertical 3-D GaN Nanowire MOSFETs with Inverted p -GaN Channel. *IEEE Transactions on Electron Devices* **65**, 2439–2445 (2018).
- Sun, M., Zhang, Y., Gao, X. & Palacios, T. High-Performance GaN Vertical Fin Power Transistors on Bulk GaN Substrates. *IEEE Electron Device Letters* **38**, 509–512 (2017).
- Liu, Z. J., Huang, T., Ma, J., Liu, C. & Lau, K. M. Monolithic Integration of AlGaIn/GaN HEMT on LED by MOCVD. *IEEE Electron Device Letters* **35**, 330–332 (2014).
- Lu, X. *et al.* Monolithic integration of enhancement-mode vertical driving transistors on a standard InGaIn/GaN light emitting diode structure. *Appl. Phys. Lett.* **109**, 053504 (2016).
- Iannaccone, G., Bonaccorso, F., Colombo, L. & Fiori, G. Quantum engineering of transistors based on 2D materials heterostructures. *Nature Nanotechnology* **13**, 183–191 (2018).
- Yu, W. J. *et al.* Vertically stacked multi-heterostructures of layered materials for logic transistors and complementary inverters. *Nature Materials* **12**, 246 (2012).

19. Kamrani, H. *et al.* Thermal performance analysis of GaN nanowire and fin-shaped power transistors based on self-consistent electrothermal simulations. *Microelectronics Reliability* **91**, 227–231 (2018).
20. Fatahlah, M. F. *et al.* Traceable Nanomechanical Metrology of GaN Micropillar Array. *Advanced Engineering Materials*, <https://doi.org/10.1002/adem.201800353> (2018).
21. Ruzzarin, M. *et al.* Instability of Dynamic- Ron and Threshold Voltage in GaN-on-GaN Vertical Field-Effect Transistors. *IEEE Transactions on Electron Devices* **64**, 3126–3131 (2017).
22. Li, W. & Chowdhury, S. Design and fabrication of a 1.2 kV GaN-based MOS vertical transistor for single chip normally off operation: Design and fabrication of a 1.2-kV GaN-based MOS vertical transistor. *physica status solidi (a)* **213**, 2714–2720 (2016).
23. Chowdhury, S., Swenson, B. L. & Mishra, U. K. Enhancement and Depletion Mode AlGaIn/GaN CAVET with Mg-Ion-Implanted GaN as Current Blocking Layer. *IEEE Electron Device Letters* **29**, 543–545 (2008).
24. Ben-Yaacov, I., Seck, Y.-K., Mishra, U. K. & DenBaars, S. P. AlGaIn/GaN current aperture vertical electron transistors with regrown channels. *Journal of Applied Physics* **95**, 2073–2078 (2004).
25. Fatahlah, M. F. *et al.* 3D GaN nanoarchitecture for field-effect transistors. *Micro and Nano Engineering* **3**, 59–81 (2019).
26. Larrieu, G. & Han, X.-L. Vertical nanowire array-based field effect transistors for ultimate scaling. *Nanoscale* **5**, 2437 (2013).
27. Son, D.-H. *et al.* Low Voltage Operation of GaN Vertical Nanowire MOSFET. **3**.
28. Yu, F. *et al.* Vertical architecture for enhancement mode power transistors based on GaN nanowires. *Applied Physics Letters* **108**, 213503 (2016).
29. Sabui, G. *et al.* (Invited) Simulation Study of High Voltage Vertical GaN Nanowire Field Effect Transistors. *ECS Transactions* **80**, 69–85 (2017).
30. Yu, F. *et al.* GaN nanowire arrays with nonpolar sidewalls for vertically integrated field-effect transistors. *Nanotechnology* **28**, 095206 (2017).
31. Hamdana, G. *et al.* Nanoindentation of crystalline silicon pillars fabricated by soft UV nanoimprint lithography and cryogenic deep reactive ion etching. *Sensors and Actuators A: Physical* **283**, 65–78 (2018).
32. Hamdana, G. *et al.* Towards fabrication of 3D isotopically modulated vertical silicon nanowires in selective areas by nanosphere lithography. *Microelectronic Engineering* **179**, 74–82 (2017).
33. Wasisto, H. S., Merzsch, S., Steib, F., Waag, A. & Peiner, E. Vertical silicon nanowire array-patterned microcantilever resonators for enhanced detection of cigarette smoke aerosols. *Micro & Nano Letters* **9**, 676–679 (2014).
34. Wasisto, H. S. *et al.* Finite element modeling and experimental proof of NEMS-based silicon pillar resonators for nanoparticle mass sensing applications. *Microsystem Technologies* **20**, 571–584 (2014).
35. Merzsch, S. *et al.* Production of vertical nanowire resonators by cryogenic-ICP-DRIE. *Microsystem Technologies* **20**, 759–767 (2014).
36. Wasisto, H. S. *et al.* Silicon resonant nanopillar sensors for airborne titanium dioxide engineered nanoparticle mass detection. *Sensors and Actuators B: Chemical* **189**, 146–156 (2013).
37. Wasisto, H. S. *et al.* Silicon Nanowire Resonators: Aerosol Nanoparticle Mass Sensing in the Workplace. *IEEE Nanotechnology Magazine* **7**, 18–23 (2013).
38. Wasisto, H. S. *et al.* Femtogram aerosol nanoparticle mass sensing utilising vertical silicon nanowire resonators. *Micro & Nano Letters* **8**, 554–558 (2013).
39. Debnath, R. *et al.* Top-down fabrication of large-area GaN micro- and nanopillars. *Journal of Vacuum Science & Technology B* **32**, 021204 (2014).
40. Dubois, V. *et al.* Massively parallel fabrication of crack-defined gold break junctions featuring sub-3 nm gaps for molecular devices. *Nature Communications* **9** (2018).
41. Siket, C. M. *et al.* Direct writing of anodic oxides for plastic electronics. *npj Flexible Electronics* **2** (2018).
42. Sun, X. *et al.* High spectral response of self-driven GaN-based detectors by controlling the contact barrier height. *Scientific Reports* **5** (2015).
43. Huang, R. *et al.* Ion Sputter Induced Interfacial Reaction in Prototypical Metal-GaN System. *Scientific Reports* **8** (2018).
44. Zhang, K., Sumiya, M., Liao, M., Koide, Y. & Sang, L. P-Channel InGaIn/GaN heterostructure metal-oxide-semiconductor field effect transistor based on polarization-induced two-dimensional hole gas. *Scientific Reports* **6** (2016).
45. Jia, Y., Wallace, J. S., Echeverria, E., Gardella, J. A. & Singiseti, U. Interface characterization of atomic layer deposited Al₂O₃ on m-plane GaN: Interface characterization of ALD-Al₂O₃ on m-plane GaN. *physica status solidi (b)* **254**, 1600681 (2017).
46. Wang, X., Brown, A. R., Binjie Cheng & Asenov, A. Statistical variability and reliability in nanoscale FinFETs. in *2011 International Electron Devices Meeting 5.4.1-5.4.4* (IEEE, 2011).
47. Han, X.-L., Larrieu, G., Dubois, E. & Cristiano, F. Carrier injection at silicide/silicon interfaces in nanowire based-nanocontacts. *Surface Science* **606**, 836–839 (2012).
48. Colinge, J.-P. *et al.* Temperature effects on trigate SOI MOSFETs. *IEEE Electron Device Letters* **27**, 172–174 (2006).
49. Qian, Q. *et al.* Improved Gate Dielectric Deposition and Enhanced Electrical Stability for Single-Layer MoS₂ MOSFET with an AlN Interfacial Layer. *Scientific Reports* **6** (2016).
50. Kaushik, N. *et al.* Reversible hysteresis inversion in MoS₂ field effect transistors. *npj 2D Materials and Applications* **1** (2017).
51. Calarco, R., Stoica, T., Brandt, O. & Geelhaar, L. Surface-induced effects in GaN nanowires. *Journal of Materials Research* **26**, 2157–2168 (2011).
52. Witzigmann, B. *et al.* Performance analysis and simulation of vertical gallium nitride nanowire transistors. *Solid-State Electronics* **144**, 73–77 (2018).
53. Fricke, L. *et al.* Self-Referenced Single-Electron Quantized Current Source. *Physical Review Letters*, **112** (2014).
54. Fricke, L. *et al.* Counting statistics for electron capture in a dynamic quantum dot. *Physical Review Letters*, **110** (2013).
55. Mnatsakanov, T. T. *et al.* Carrier mobility model for GaN. *Solid-State Electronics* **47**, 111–115 (2003).

Acknowledgements

The authors would like to thank A. Schmidt, J. Breifelder, M. Rühmann, and K.-H. Lachmund for their valuable technical assistances. Authors are also grateful for the planar GaN wafers provided by the members of epitaxy competence center (ec²) of TU Braunschweig (I. Mangano Clavero and C. Margenfeld). This work has been performed within the projects of ‘LENA-OptoSense’ funded by the Lower Saxony Ministry for Science and Culture (MWK) and ‘3D Concepts for Gallium-Nitride Electronics (3D GaN)’ funded by the German Research Foundation (DFG). Support by Ministry of Research, Technology, and Higher Education of the Republic of Indonesia (RISTEKDIKTI) and Indonesian-German Center for Nano and Quantum Technologies (IG-Nano) is also acknowledged. The research activity at University of Padova was partly funded by project “Novel vertical GaN-devices for next generation power conversion”, NoveGaN (University of Padova), through the STARS CoG Grants call.

Author Contributions

M.F.F. designed, fabricated, and characterized the *n-p-n* vertical GaN NW FETs. M.F.F., F.Y., and K.S. analyzed the realized FETs. A.B., F.Y., and K.S. supported the ALD process of the dielectric materials. K.S. provided the *n-p-n* GaN wafers and performed the FE-SEM analysis. D.M. characterized the fabricated FETs. F.R. and B.W. provide simulation and theory of the fabricated FETs. M.F.F., K.S., F.Y., F.R. and H.S.W. wrote the manuscript. H.S.W., A.W., B.W., M.M., F.H, and H.W.S. provided significant inputs on fabrication and characterization of FETs. A.W. and H.S.W. led the development of the vertical GaN NW FETs and coordinated the projects. All authors reviewed the manuscript.

Additional Information

Supplementary information accompanies this paper at <https://doi.org/10.1038/s41598-019-46186-9>.

Competing Interests: The authors declare no competing interests.

Publisher's note: Springer Nature remains neutral with regard to jurisdictional claims in published maps and institutional affiliations.



Open Access This article is licensed under a Creative Commons Attribution 4.0 International License, which permits use, sharing, adaptation, distribution and reproduction in any medium or format, as long as you give appropriate credit to the original author(s) and the source, provide a link to the Creative Commons license, and indicate if changes were made. The images or other third party material in this article are included in the article's Creative Commons license, unless indicated otherwise in a credit line to the material. If material is not included in the article's Creative Commons license and your intended use is not permitted by statutory regulation or exceeds the permitted use, you will need to obtain permission directly from the copyright holder. To view a copy of this license, visit <http://creativecommons.org/licenses/by/4.0/>.

© The Author(s) 2019